

X-ray Observations of Luminous Dusty Quasars at $z > 2$

G. B. Lansbury,^{1,2*} M. Banerji,^{1,3} A. C. Fabian¹ and M. J. Temple¹

¹*Institute of Astronomy, University of Cambridge, Madingley Road, Cambridge, CB3 0HA, UK*

²*European Southern Observatory, Karl-Schwarzschild str. 2, 85748 Garching bei München, Germany*

³*Kavli Institute for Cosmology, University of Cambridge, Madingley Road, Cambridge CB3 0HA, UK*

29 April 2020

ABSTRACT

We present new X-ray observations of luminous heavily dust-reddened quasars (HRQs) selected from infrared sky surveys. HRQs appear to be a dominant population at high redshifts and the highest luminosities, and may be associated with a transitional “blowout” phase of black hole and galaxy co-evolution models. Despite this, their high-energy properties have been poorly known. We use the overall sample of 10 objects with *XMM-Newton* coverage to study the high-energy properties of HRQs at $\langle L_{\text{bol}} \rangle = 10^{47.5}$ erg s⁻¹ and $\langle z \rangle = 2.5$. For seven sources with strong X-ray detections, we perform spectral analyses. These find a median X-ray luminosity of $\langle L_{2-10\text{keV}} \rangle = 10^{45.1}$ erg s⁻¹, comparable to the most powerful X-ray quasars known. The gas column densities are $N_{\text{H}} = (1-8) \times 10^{22}$ cm⁻², in agreement with the amount of dust extinction observed. The dust to gas ratios are sub-Galactic, but are higher than found in local AGN. The intrinsic X-ray luminosities of HRQs are weak compared to the mid-infrared ($L_{6\mu\text{m}}$) and bolometric luminosities (L_{bol}), in agreement with findings for other luminous quasar samples. For instance, the X-ray to bolometric corrections range from $\kappa_{\text{bol}} \approx 50-3000$. The moderate absorption levels and accretion rates close to the Eddington limit ($\langle \lambda_{\text{Edd}} \rangle = 1.06$) are in agreement with a quasar blowout phase. Indeed, we find that the HRQs lie in the forbidden region of the $N_{\text{H}}-\lambda_{\text{Edd}}$ plane, and therefore that radiation pressure feedback on the dusty interstellar medium may be driving a phase of blowout that has been ongoing for a few 10^5 years. The wider properties, including [O III] narrow-line region kinematics, broadly agree with this interpretation.

Key words: galaxies: evolution – galaxies:active – galaxies: nuclei – quasars: general – X-rays: galaxies

1 INTRODUCTION

Growing supermassive black holes (i.e., active galactic nuclei; AGNs) at the centers of galaxies have an enormous energy output from accretion, and are thus expected to play a role in the growth of galaxies. Indeed, tight relations are observed between properties of black holes and their hosts (e.g., Magorrian et al. 1998; Ferrarese & Merritt 2000; Gebhardt et al. 2000), and theoretical simulations require AGNs to reproduce the observed properties of massive galaxies (e.g., Springel et al. 2005; Bower et al. 2006). A key observational prediction from simulations is that many of the most rapidly growing supermassive black holes (i.e., luminous quasars) are enshrouded in gas and dust, and thus obscured at bluer wavelengths but visible in the infrared through reprocessed dust emission (e.g., Sanders & Mirabel 1996; Hopkins et al. 2008; Narayanan et al. 2010; Hickox & Alexander 2018).

The rapid accretion should result in a transitional reddened quasar phase during which the gas and dust, fuel for stellar and black hole growth, are being catastrophically disrupted or expelled from the galaxy. Following this phase of quasar feedback, the central engine may be more readily observable as an unobscured quasar.

If high columns of dust are present around a rapidly accreting black hole, outflows are expected to be driven by radiation pressure (e.g., Murray et al. 2005; Fabian et al. 2008; Debuhr et al. 2011; Fabian 2012), which can strongly influence the structure and kinematics of circumnuclear and galactic material (e.g., Hönig & Kishimoto 2017; Costa et al. 2018; Hönig 2019). Evidence of the influence of such processes can be found in low-redshift X-ray samples, which provide a relatively clean sampling of the AGN population. In particular, these samples show an absence of objects with high Eddington ratios ($\lambda_{\text{Edd}} = L_{\text{bol}}/L_{\text{Edd}} \gtrsim 0.1$) and moderate gas column densities of $\log(N_{\text{H}}/\text{cm}^{-2}) \approx 22-23.5$ (e.g., Fabian et al. 2009; Raimundo et al. 2010; Va-

* E-mail: george.lansbury@eso.org

sudevan et al. 2013; Ricci et al. 2017b; Liu et al. 2018; Bär et al. 2019). This is in agreement with models of radiation pressure feedback on circumnuclear dusty gas (e.g., Fabian et al. 2006; Ishibashi et al. 2018), which predict a “forbidden” or “blowout” region in the $\lambda_{\text{Edd}}\text{--}\mathcal{N}_{\text{H}}$ plane, in which AGN are rarely observed. The lack of objects discovered in this blowout region to-date may partly result from the poor sampling of luminous quasars accreting close to the Eddington limit, and with high dust columns (e.g., Raimundo et al. 2010). Glikman (2017) has already shown that some luminous red quasars at $z < 1$ lie in the forbidden region. It is crucial to expand such study to the most luminous quasars at their peak epoch of activity ($z \sim 2\text{--}3$; e.g., Richards et al. 2006).

Following the advent of sensitive large-area optical and infrared surveys of the sky, a number of luminous reddened quasar samples have been discovered, which may be fundamentally different from blue quasars (e.g., Klindt et al. 2019). In particular, objects with red colours have been identified in the *WISE* all-sky imaging survey (e.g., Eisenhardt et al. 2012; Hainline et al. 2014; Tsai et al. 2015; Assef et al. 2015), in ground-based near-infrared (NIR) imaging surveys (e.g., Banerji et al. 2012, 2013, 2015; Temple et al. 2019), in the SDSS (e.g., Richards et al. 2003; Ross et al. 2015), and among radio loud objects in the 2MASS survey (e.g., Glikman et al. 2007, 2015). These samples include hyperluminous quasars at $z \gtrsim 2$. At these high redshifts, there is tentative evidence for an increase in the typical obscuring column around luminous AGNs (e.g., Aird et al. 2015), and the aforementioned radiative feedback processes are expected to be common.

A large sample of $z \gtrsim 2$ red quasars with spectroscopically identified broad emission lines has been obtained from a coordinated effort (Banerji et al. 2015; Temple et al. 2019) selecting and following up red objects from multiple wide-field ($\gtrsim 1000 \text{ deg}^2$ in total) NIR surveys: the UKIDSS Large Area Survey (ULAS; Lawrence et al. 2007); the European Southern Observatory (ESO) VISTA Hemisphere Survey (VHS; McMahon et al. 2013); and the ESO VISTA Kilo-degree Infrared Galaxy survey (VIKING; Edge et al. 2013). This work has revealed a population of heavily reddened quasars (“HRQs” hereafter) which have measured extinctions of $0.5 \lesssim E_{B-V} \lesssim 2.0$ (see Section 3.2), and are therefore typically not detectable in wide-field optical surveys. The high dust extinctions and luminosities may correspond to an enhanced phase of AGN feeding, and possibly feedback. Importantly, at the high end of the AGN luminosity function ($L_{\text{bol}} \gtrsim 10^{47} \text{ erg s}^{-1}$) HRQs are at least as numerous as unobscured optical (e.g., SDSS) quasars (Banerji et al. 2015). It is thus of importance to constrain their physical properties, and better understand this significant phase of black hole growth in the Universe.

HRQs are compelling laboratories in which to study the accretion environment around rapidly growing supermassive black holes during their peak epoch of growth. From a practical perspective, the obscuring columns are sufficiently low that the broad line region is still observable and the continuum is detected, thus allowing constraints on black hole mass, bolometric luminosity, and accretion rate. From a physical perspective, HRQs appear to be dusty and accreting at a significant fraction of the Eddington limit (e.g., Temple et al. 2019), meaning that AGN feedback is likely

to be having a significant impact. Despite this, their high-energy properties are poorly known, with only three objects having been studied in the X-ray band (e.g., Banerji et al. 2014; Martocchia et al. 2017), and it is unclear how they fit in with luminous unobscured quasars (e.g., Just et al. 2007; Stern 2015; Martocchia et al. 2017) and other luminous reddened quasars studied at high energies (e.g., LaMassa et al. 2016b; Glikman et al. 2017; Goulding et al. 2018; Vito et al. 2018a; Zappacosta et al. 2018).

X-ray photons are emitted from an extremely hot plasma (the corona) within ~ 10 gravitational radii of the black hole (e.g., Fabian et al. 2015). Imprinted on the observed X-ray spectrum, therefore, are the features of absorption and scattering by matter along an almost direct line to the black hole. It is thus possible to obtain an accurate measurement of the line-of-sight gaseous column density (\mathcal{N}_{H}) and the intrinsic (i.e., absorption-corrected) luminosity. This makes possible: (i) constraints on the makeup and location of the obscuring media, when comparing to dust extinction; (ii) insight into the physics of the X-ray corona, when comparing to infrared–ultraviolet emission; and (iii) tests of AGN feedback models, when comparing to the accretion rates and outflow properties.

In this paper we report on new X-ray observations which, in combination with archival data, allow us to characterise the high-energy properties of the HRQ population, and begin to address (i)–(iii) above. Section 2 describes the sample, the observations, and the data processing and analysis procedures. In Section 3 we present and discuss the results: measurements of X-ray properties (Section 3.1); dust versus gas obscuration (Section 3.2); a comparison between the intrinsic X-ray, infrared, and bolometric accretion luminosities (Section 3.3); and the $\mathcal{N}_{\text{H}}\text{--}\lambda$ plane for HRQs, in the context of radiation pressure feedback models (Section 3.4). In Section 3.5 we consider how the results can be understood in the context of other hyperluminous quasar samples. Section 4 summarises the main results. We adopt cosmological parameters of $(\Omega_M, \Omega_\Lambda, h) = (0.27, 0.73, 0.70)$.

2 THE SAMPLE AND DATA

2.1 The parent sample

Our parent sample of highly luminous heavily dust-reddened type 1 quasars (HRQs) was selected from the large-area ($\gtrsim 1000 \text{ deg}^2$) infrared photometric survey catalogs ULAS (Lawrence et al. 2007), VHS (McMahon et al. 2013), and VIKING (Edge et al. 2013). The overall approach of the previous studies (Banerji et al. 2012, 2015; Temple et al. 2019) was to identify objects with extremely red NIR colours, and then perform subsequent spectroscopic followup to confirm the HRQ candidates as quasars, and accurately determine redshifts. The sources considered here have $(J - K)_{\text{Vega}} > 2.5$ or $(H - K)_{\text{Vega}} > 1.9$, and $K_{\text{Vega}} < 17.5$. They are AGN-dominated in the mid-infrared, based on a *WISE* color selection of $(W1 - W2) > 0.85$. Additionally, six of the sources presented here were also required in their initial selections to have optical non-detections, faint optical magnitudes, and/or red optical–NIR colors of at least $(i - K)_{\text{Vega}} > 4.4$ (for J1234, J1539, and J2200, refer to Section 2.1 of Banerji et al. 2012; for J2205, J2243, and J2314, refer to Section 2.1.2 of Temple et al. 2019).

2.2 The X-ray sample and observations

We consider all spectroscopically confirmed HRQs at $z > 2$ that have coverage from sensitive X-ray telescopes. There are ten such quasars, all with coverage from *XMM-Newton*, detailed in Table 1. For five of these sources (J1122, J2200, J2205, J2243, and J2314), the quasars were targetted as part of a new *XMM-Newton* program (PI Lansbury; program ID 082409), which targetted sources with luminous [O III] line detections ($L_{[\text{OIII}]} > 10^{43} \text{ erg s}^{-1}$) from Temple et al. (2019). J1234 and J2315 were targetted through our previous programs (PI McMahon and Banerji, respectively), with the former data published in Banerji et al. (2014). J0144 was covered as part of the Stripe 82 X-ray survey (LaMassa et al. 2016a), J1216 was detected off-axis in an archival observation (PI Ponman), and J1539 was targetted (PI Zappacosta) and published in Martocchia et al. (2017).

The ten X-ray observed HRQs have redshifts in the range $z = 2.085\text{--}2.658$, and a median redshift of $\langle z \rangle = 2.503$. All objects have broad emission lines in their optical spectra, but are heavily reddened with $0.53 < E_{B-V} < 1.94$. Sources with $E_{B-V} \gtrsim 1$ are among the dustiest broad-line type 1 quasars known. The black hole masses are in the range $8.4 < \log M_{\text{BH}} < 10.5$, with a median value of 9.4 (Temple et al. 2019). The infrared luminosity at $6 \mu\text{m}$, which traces the intrinsic AGN power, has a median value of $\langle \log(L_{6\mu\text{m}}/\text{erg s}^{-1}) \rangle = 46.64$. These sources are therefore some of the most bolometrically luminous quasars.

2.3 X-ray data processing and analyses

We process data from the *XMM-Newton* Pipeline Processing System, using the *XMM-Newton* Science Analysis Software (SAS v17.0.0). To further clean the data, we examine the background count-rate lightcurves above 10 keV and exclude time intervals of significant background flaring. For PN we make this flaring cut using rate thresholds between < 0.4 and $< 1 \text{ s}^{-1}$, and for MOS we use $< 0.4 \text{ s}^{-1}$. Table 1 lists the net exposure times following the flaring correction.

For the photometric and spectral analyses we adopt as standard source regions with radii of 15 arcsec, centered on the NIR source position. For the two most strongly detected sources we use 20 arcsec. In each case, we extract the background from a large-area (between 2 and 18 sq. arcmin) source-free region nearby, but not contaminated by, the quasar.

2.3.1 Source detections and photometry

We produce images in multiple observed-frame and rest-frame energy bands. For individual images, we extract the total counts from the source region (S) and from the background region (B), and apply established aperture photometry procedures (e.g., Lansbury et al. 2014) to determine: the binomial no-source probability (P_B); the net background-subtracted source counts (S_{net}) and associated Poisson errors; and 3σ upper limits to S_{net} for non-detections (Kraft et al. 1991).

Seven out of ten sources are clearly strong detections in the *XMM-Newton* images (Figure 1). Table 1 lists the measured values of S and S_{net}/S . For subsequent analyses of these

sources, we limit to the energy ranges where there is significant signal above the background: 0.2–10 keV for J1234, J2200, and J2315; 0.2–4.5 keV for J2243; 0.5–10 keV for J1216 and J1539; and 0.5–4.5 keV for J2314. We constrain the X-ray properties (e.g., luminosities) of these sources using spectral modelling (Sections 2.3.2 and 3.1).

Of the remaining three out of ten sources, two (J1122 and J2205) are undetected at all energies, and one (J0144) has a weak detection. J0144 is confirmed to be significantly detected in the $\approx 0.5\text{--}3$ keV sub-band ($P_B \ll 1\%$), but not at higher energies. We characterise these three sources using photometry, as spectral modelling is not feasible. To convert the S_{net} constraints to count rates, we divide by exposure times drawn from exposure maps produced using EEXPMAP, thus accounting for spatially variable sensitivity (e.g., vignetting). We divide by encircled energy fractions determined from PSFGEN simulations, to correct to the 100% PSF flux and to account for off-axis effects. To convert from count rates to fluxes, we use PIMMS-based conversion factors which assume a power-law spectrum with a photon index of $\Gamma = 1.7$ and a Galactic column density of $N_{\text{H}} = 3 \times 10^{20} \text{ cm}^{-2}$. To obtain X-ray luminosity constraints in the rest-frame 2–10 keV band, we perform the above photometry in the appropriate observed-frame band (e.g., 0.57–2.9 keV for J0144, at $z = 2.5$), thus eliminating the need for extrapolations between bands. We also performed photometry at higher rest-frame energies (e.g., 10–40 keV) but found that the additional information (e.g., upper limits and band ratios) obtained do not significantly improve the characterisation of these three sources.

2.3.2 Spectroscopy

For the spectral modelling of the seven well detected sources, we extract spectral products (spectra and response files) using the source and background regions above. The individual MOS spectra are combined using EPICSPCCOMBINE. We group the spectra by a minimum of one count per bin, and model them using XSPEC (version 12.10.1h; Arnaud 1996), using the W -statistic for fitting. This is recommended for the low counts regime, and gives results consistent with χ^2 fitting at high counts. We model the PN and MOS spectra simultaneously. We fit the spectra with simple absorbed power law models that account for photoelectric absorption and Compton-scattering out of the line-of-sight (`cabs · zwabs · pow` in XSPEC formalism). We account for the low-level absorption through the Galaxy with additional multiplicative absorption components fixed to values from Kalberla et al. (2005).

Since the column densities (Section 3) appear to be low, the X-ray spectra are dominated by the transmitted continuum, and therefore additional light from Compton scattering by distant material is not expected to contribute significantly. Therefore, fitting with more detailed physically motivated (e.g., torus) models is unlikely to change the main parameter constraints. Nevertheless, we perform additional fitting using the torus model of Baloković et al. (2018) in a standard setup with the toroidal column density uncoupled from the line-of-sight one.

Table 1. Summary of the *XMM-Newton* data used for spectral (and photometric) analyses

Object (1)	R.A. (2)	Decl. (3)	z (4)	Obs ID (5)	UT Date (6)	t_{on} [ks] (7)	t [ks] (8)	S [cts] (9)	S_{net}/S [%] (10)
ULAS J0144–0014	01:44:52.00	−00:14:32.2	2.504	0747440131	2014-08-04	9.5/11.8	3.5/4.8	26/13	58.0/63.0
VHS J1122–1919	11:22:24.43	−19:19:17.4	2.464	0824090201	2018-07-10	15.8/17.6	9.6/16.8	74/49	<35.4/<36.9
ULAS J1216–0313	12:16:31.77	−03:13:35.0	2.574	0305800701	2005-12-16	18.0/26.5	1.8/4.1	36/22	86.0/87.2
ULAS J1234+0907	12:34:27.52	+09:07:54.2	2.502	0722960101	2013-06-30	51.0/52.6	41.8/51.6	528/377	76.4/81.7
ULAS J1539+0557	15:39:10.16	+05:57:49.7	2.658	0745010101	2015-02-16	42.7/44.6	29.5/37.2	261/226	80.7/84.2
ULAS J2200+0056	22:00:24.87	+00:56:04.7	2.541	0824090801	2018-11-28	8.6/13.8	7.3/13.5	210/203	75.9/84.0
VIK J2205–3132	22:05:13.68	−31:32:02.4	2.307	0824090301	2018-11-10	42.7/2.8	15.5/...	49/...	<36.3/...
VIK J2243–3504	22:43:48.96	−35:04:39.4	2.085	0824090401	2018-11-16	22.5/31.5	19.2/30.8	395/336	74.4/84.4
VIK J2314–3459	23:14:16.87	−34:59:47.0	2.325	0824090501	2018-11-14	20.3/33.7	17.4/32.9	70/105	53.1/33.4
ULAS J2315+0143	23:15:56.23	+01:43:50.3	2.560	0745320101	2014-12-16	54.0/54.1	28.3/47.4	896/1072	88.3/82.5

Notes. (1): Object name. (2) and (3): The position of the source in the NIR sky survey, in J2000 coordinates. (4): Spectroscopic redshift. (5) and (6): *XMM-Newton* observation ID and date. (7): Total on-axis exposure times for PN and MOS respectively, before filtering. (8): Net exposure times at the source position, accounting for flaring-subtraction and vignetting. (9): Source counts at 2–10 keV, within the source extraction region (S). For J0144 and J1216, the MOS values are for M2 only. (10): The ratio of net background-subtracted source counts (S_{net}) to the total source counts. Upper limits indicate non-detections.

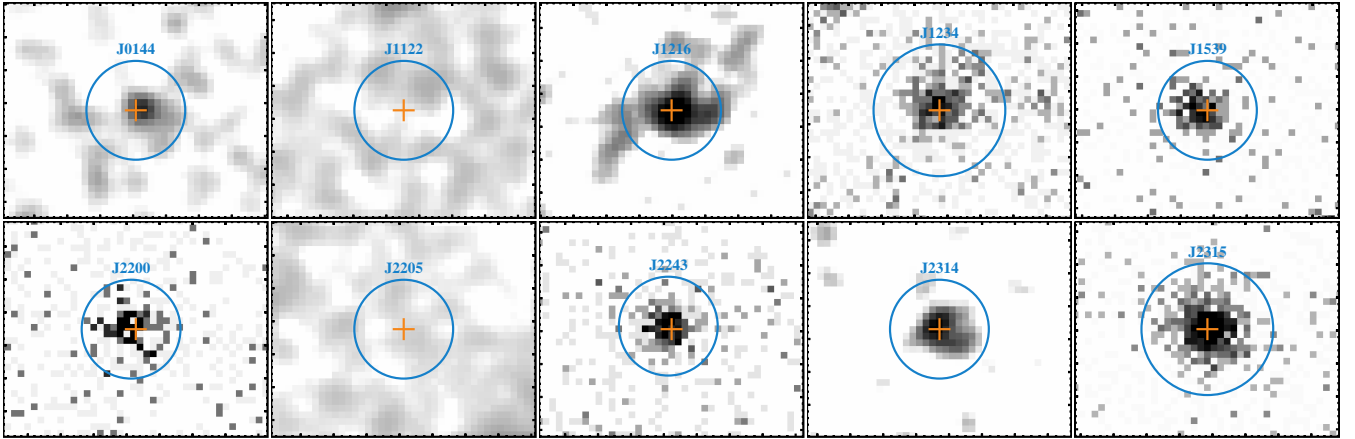


Figure 1. *XMM-Newton* images at $E = 0.5\text{--}10$ keV from the PN camera for each of the HRQs in this work. The near-infrared (NIR) source positions are marked by orange crosses, and the extraction regions used for X-ray spectroscopy and photometry are shown as blue circles. The images are binned to 2 arcsec per pixel. For the five strongest and weakest detections we show unsmoothed and smoothed data (with a gaussian of 3-pixel width), respectively. The axes major ticks show steps of 10 arcsec.

3 RESULTS AND DISCUSSION

3.1 X-ray properties

Given the high redshifts, and the *XMM-Newton* sensitivity window, it has been possible to access energies of $E \approx 0.7\text{--}35$ keV in the source rest-frame. This means that the relatively unabsorbed high-energy part of the X-ray spectrum lies within the observed band, and the intrinsic accretion power and spectral shapes of the quasars can be reliably measured.

For the seven strongly detected sources, we find that the spectra are well described by simple absorbed power law models with no additional components (see Table 2 and Figure 2). In six cases, it is possible to simultaneously constrain N_{H} and the intrinsic photon index (Γ). In the seventh case (J2314) Γ was fixed to 1.9, consistent with the average for the sample. The measured column densities are in the range $N_{\text{H}} = (1.0\text{--}4.2) \times 10^{22} \text{ cm}^{-2}$ (Table 2). For J1234, J1539, and

J2315 the column densities measured are in agreement with previous works, which also used simple absorbed power law models, within the uncertainties (Banerji et al. 2014; Mar-tocchia et al. 2017). For one source (J1216), the fitting only places an upper limit on N_{H} . This source and J0144 are both detected off-axis, and have small net exposure times; their physical constraints would be significantly improved with further *XMM-Newton* observations of modest exposure time.

The intrinsic (i.e., unabsorbed) power-law spectra of the modelled HRQs have photon indices which appear broadly consistent with the typical range for AGNs (i.e., $\bar{\Gamma} \approx 1.8$, $\sigma_{\Gamma} \approx 0.2$; e.g., Alexander et al. 2013; Rivers et al. 2013; Ricci et al. 2017a). The mean intrinsic photon index for the HRQs with constrained values is $\bar{\Gamma} = 1.88$. The most significant outlier is J2243, with $\Gamma = 2.5 \pm 0.3$. The intrinsic luminosities in the rest-frame 2–10 keV band cover the range $\log(L_{2\text{--}10\text{keV}}/\text{erg s}^{-1}) = 44.4\text{--}45.6$, with a median of 45.1. This confirms that the central engines of HRQs are ex-

Table 2. X-ray properties

Object (1)	Γ (2)	N_{H} (3)	$L_{\text{X}}^{\text{obs}}$ (4)	$L_{\text{X}}^{\text{int}}$ (5)	W/n (6)
J0144	...	1.4^{\dagger}	44.7	44.7^{\dagger}	...
J1122	...	2.3^{\dagger}	< 44.3	$< 44.3^{\dagger}$...
J1216	$1.7^{+0.3}_{-0.1}$	< 8.0	45.3	45.3	50/54
J1234	$1.8^{+0.1}_{-0.1}$	$2.1^{+0.8}_{-0.7}$	45.0	45.1	499/572
J1539	$1.6^{+0.2}_{-0.1}$	$4.2^{+1.7}_{-1.5}$	45.0	45.1	332/386
J2200	$1.9^{+0.2}_{-0.1}$	$1.0^{+0.5}_{-0.5}$	45.4	45.5	294/335
J2205	...	1.2^{\dagger}	< 44.0	$< 44.1^{\dagger}$...
J2243	$2.5^{+0.2}_{-0.2}$	$1.8^{+0.4}_{-0.3}$	45.1	45.1	336/469
J2314	[1.9]	$3.8^{+3.0}_{-2.1}$	44.3	44.4	99/120
J2315	$1.8^{+0.1}_{-0.1}$	$1.3^{+0.2}_{-0.2}$	45.5	45.6	803/888

Notes. (1) Short object name. (2): Photon index for the intrinsic (i.e., unabsorbed) X-ray power law spectrum, and the associated 1σ errors. (3): Gas column density in units of 10^{22} cm^{-2} , and 1σ errors. (4) and (5): Logarithm of the observed and intrinsic luminosities in the rest-frame 2–10 keV energy band. (6) Ratio of the W -statistic value to the number of degrees of freedom. \dagger : Estimates based on the average E_{B-V}/N_{H} .

tremely powerful. As shown in Section 3.3, when comparing to some of the most luminous quasars known in the Universe, the X-ray luminosities of the HRQs are in most cases comparably high.

Fitting instead with the physically motivated toroidal model of Baloković et al. (2018), the best-fit results for N_{H} , Γ , and L_{X} agree closely with those above, within the errors, and there is no statistical improvement in the fits. Since the best-fit models are dominated by the primary transmitted X-ray continuum, there are no informative constraints on toroidal or geometric parameters.

3.2 Dust versus gas

Comparison of the gaseous column density (N_{H}) with the dust reddening (E_{B-V}) can provide clues as to the nature of the absorbing media in the HRQs. In Figure 3 we plot the ratios of E_{B-V}/N_{H} for the seven HRQs with strong X-ray detections. The E_{B-V} values were measured from the NIR photometry by Temple et al. (2019) for eight objects, and by Banerji et al. (2012) for J1539. For the tenth object, J2315, we adopt the value from Wethers et al. (2018) based on fitting of the optical-NIR SED. We find that the ratios range between $10^{-22.9}$ and $10^{-22.0}$, with an average of $E_{B-V}/N_{\text{H}} = 10^{-22.3}$. For comparison, we also plot the Galactic value of $E_{B-V}/N_{\text{H}} = 10^{-21.8}$ (Savage & Mathis 1979; Güver & Özel 2009). Although ≈ 3 sources are consistent with the Galactic value, there is a systematic offset suggesting that HRQs have slightly lower dust to gas ratios than the Galaxy.

Despite this offset, the HRQs in fact deviate less from the Galactic value than local AGNs (e.g., Maiolino et al. 2001; Burtscher et al. 2016; Shimizu et al. 2018; see Figure 3) and compared to some other luminous high-redshift quasars (see Section 3.5). Four other red quasars at $z \approx 0.1$ – 0.7 (selected from FIRST and 2MASS; ‘‘F2M’’ quasars hereafter) studied in the X-ray band by LaMassa et al. (2016b) and Glikman et al. (2017) have a distribution of E_{B-V}/N_{H} values broadly consistent with our HRQ sample (black points in

Figure 3), although the average may be slightly lower. For the local AGNs (grey points in Figure 3), the highly sub-Galactic E_{B-V}/N_{H} values typically observed are thought to result, at least partly, from excess X-ray absorption due to neutral dust-free gas in the innermost \approx sub-parsec regions (e.g., Merloni et al. 2014; Davies et al. 2015; Burtscher et al. 2016; Shimizu et al. 2018; Liu et al. 2018). One interpretation for the HRQs and the F2M red quasars, therefore, is that they are less dominated by absorption from the innermost regions. The HRQ obscurers then have a higher dust content, with the dust and gas columns associated with material on similar physical scales, potentially at larger radial distances from the central black hole ($\gtrsim 100$ pc). Dust in HRQs has previously been suggested to be distributed on large scales, based on the narrow-line region (NLR) properties (Temple et al. 2019) and the identification of galaxy-scale dust emitting regions in a few HRQs (Banerji et al. 2018). A variability study, using multi-epoch X-ray observations, would help to better establish the location of the gaseous obscuring media.

3.3 X-ray versus infrared and bolometric luminosities

The NIR-selected HRQs have extremely high infrared and bolometric luminosities (medians of $\langle L_{6\mu\text{m}} \rangle = 10^{46.6}$ and $\langle L_{\text{bol}} \rangle = 10^{47.5} \text{ erg s}^{-1}$, respectively). Here we compare these to the measured X-ray luminosities ($\langle L_{2-10} \rangle = 10^{45.1} \text{ erg s}^{-1}$) in order to test scaling relations at the highest luminosities in the AGN population, and to better understand the HRQs in the context of other powerful quasar samples.

The X-ray emission from AGNs arises from a corona, close to the innermost region of accretion, whilst mid-infrared emission is thought to arise from distant circum-nuclear dust which reprocesses accretion disk photons. The X-ray luminosities and the mid-infrared (e.g., $6 \mu\text{m}$) luminosities of AGNs are known to follow a correlation, which has been characterised using many different samples (e.g., Figure 4; Lutz et al. 2004; Fiore et al. 2009; Gandhi et al. 2009; Lanzuisi et al. 2009; Levenson et al. 2009; Ichikawa et al. 2012; Weedman et al. 2012; Asmus et al. 2015; Mateos et al. 2015; Stern 2015; Carrera et al. 2017; Chen et al. 2017; Toba et al. 2019). Importantly, when the highest luminosities are considered ($L_{6\mu\text{m}} \gtrsim 45.5 \text{ erg s}^{-1}$), there appears to be deviation from a constant ratio of $L_{\text{X}}:L_{6\mu\text{m}}$, such that the most luminous objects show relatively weak X-ray emission. This has led to the calibration of luminosity-dependent relations (e.g., Stern 2015; Chen et al. 2017).

Figure 4 shows our HRQ sample compared to various measurements of the $L_{\text{X}}-L_{6\mu\text{m}}$ relation and to other luminous quasar samples, both reddened and unobscured. For the seven sources with constraints from X-ray spectral modelling, we are able to show the intrinsic (i.e., absorption corrected) X-ray luminosities. For the remaining three sources (two of which are non-detections), we only show constraints on the observed (i.e., absorbed) X-ray luminosities. The intrinsic X-ray luminosity constraints for these three sources should however lie close to the observed X-ray luminosities, assuming their dust to gas ratios are similar to the overall sample, and their N_{H} values thus lie close to the estimates in Table 2. Alternatively, these sources (J1122

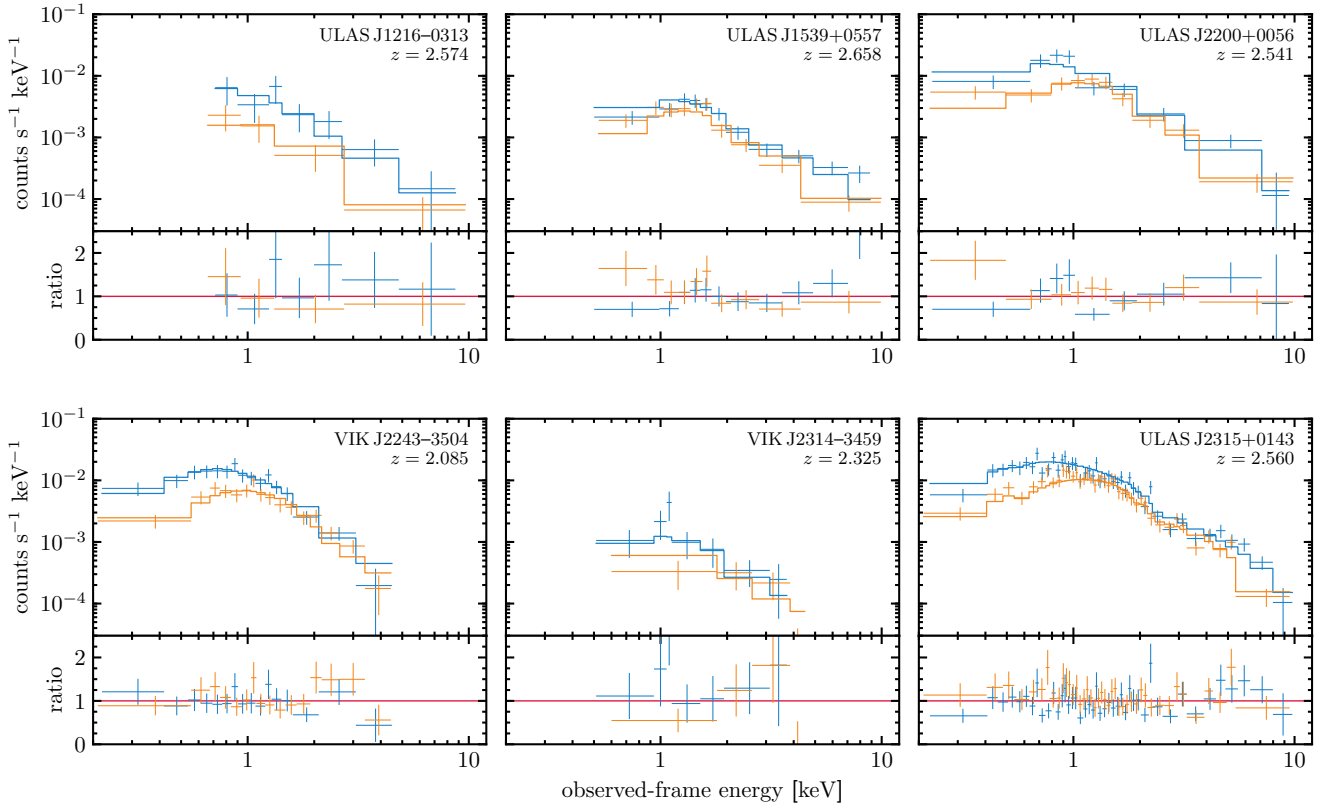


Figure 2. X-ray spectra and data/model ratios for six HRQs with sufficient counts for spectral modelling. The seventh such object, J1234, was presented in [Banerji et al. \(2014\)](#). The photon energies shown are in the observed frame. Given the redshifts of the objects, the full range of rest-frame energies sampled is 0.7–35 keV. The best-fitting absorbed power-law models are shown as solid lines, binned to match the data. For visual purposes, the data are binned by 2σ per bin for J1216 and J2314, and 4σ for the remainder. Data from the PN and MOS cameras are coloured as blue and orange, respectively.

and J2205 in particular) could be outlying highly obscured ($N_{\text{H}} \gtrsim 10^{23} \text{ cm}^{-2}$) HRQs with anomalous low dust to gas ratios. The rest-frame $6 \mu\text{m}$ luminosities ($L_{6\mu\text{m}}$) shown were determined from the *WISE* photometry: for eight sources with detections in all *WISE* photometric bands, $L_{6\mu\text{m}}$ was obtained from interpolation between the W3 and W4 bands; for the two sources undetected in the W4 band (J2205 and J2314), $L_{6\mu\text{m}}$ was estimated from the W3 flux.

Considering the results for the overall sample, the HRQs do indeed have intrinsic X-ray to infrared luminosity ratios which are significantly lower than observed for lower redshift, lower luminosity AGN (e.g., [Lutz et al. 2004](#); [Gandhi et al. 2009](#); [Asmus et al. 2015](#)), but are in better agreement with ratios that consider high luminosity AGNs (e.g., [Fiore et al. 2009](#); [Lanzuisi et al. 2009](#); [Stern 2015](#); [Chen et al. 2017](#); [Martocchia et al. 2017](#); [Goulding et al. 2018](#); but see also [Mateos et al. 2015](#)). The luminosity dependence may be connected to, or driven by, the underlying relationship between X-ray and bolometric optical/UV emission, where X-ray emission again becomes relatively weak at the highest luminosities and accretion rates, due to a saturation or disruption of the X-ray emitting plasma (e.g., [Ricci et al. 2017c](#); [Bañados et al. 2018](#)).

The HRQs additionally show some evidence for intrinsic X-ray weakness (e.g., [Luo et al. 2014](#); [Teng et al. 2014](#); [Vito et al. 2018b](#)), on average, with respect to other typ-

ical AGNs of the same infrared luminosity. For instance, eight (out of 10) of the HRQs lie below the relation of [Stern \(2015\)](#). At a given infrared luminosity, their X-ray luminosities cover a range of up to ≈ 1 dex, suggesting diversity in the X-ray properties of a population selected on relatively uniform infrared properties. We additionally note that the amount of scatter seen around the scaling relations is similar to that seen for hyperluminous unobscured quasars (e.g., [Martocchia et al. 2017](#)), especially when the three weakly and undetected X-ray sources are excluded (J0144, J1122, and J2205).

As mentioned, the X-ray emission of AGNs is also observed to weaken with increasing accretion power, relative to the bolometric luminosity inferred from the optical continuum (L_{bol}). This manifests as a positive relation between the X-ray to bolometric correction ($\kappa_{\text{bol}} = L_{\text{bol}}/L_{2-10}$) and the Eddington ratio ($\lambda_{\text{Edd}} = L_{\text{bol}}/L_{\text{Edd}}$; e.g., [Elvis et al. 1994](#); [Vasudevan & Fabian 2007](#); [Vasudevan et al. 2009](#); [Lusso et al. 2012](#)). For the HRQs, bolometric luminosities have been estimated from the optical continuum luminosities at rest-frame 5100 \AA ([Temple et al. 2019](#)). Figure 5 shows our sample in κ_{bol} versus λ_{Edd} , compared to the relation measured for AGNs by [Lusso et al. \(2012\)](#). We find that for four of the HRQs the bolometric corrections are within the expected range given their Eddington ratios, with $\kappa_{\text{bol}} = 47\text{--}105$. However, the remaining six HRQs have apparently high

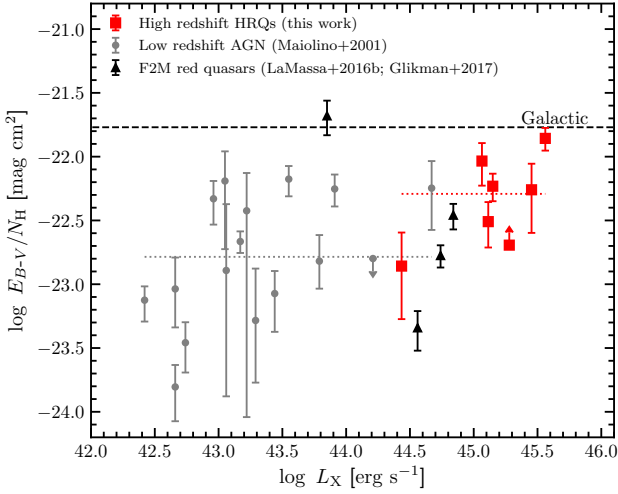


Figure 3. The ratio of dust-reddening (E_{B-V}) to gas column density (N_{H}) as a function of intrinsic 2–10 keV luminosity (L_{X}). The dashed line shows the ratio found for the Galaxy (Savage & Mathis 1979; Güver & Özel 2009). Dotted lines show the average ratios for for lower luminosity AGNs at $z < 0.7$ (grey; Maiolino et al. 2001) and for our luminous $z \approx 2.5$ HRQs (red). We also compare with $z \approx 0.5$ F2M red quasars (black data points; LaMassa et al. 2016b; Glikman et al. 2017). For the HRQs and red quasars, we include both the measurement uncertainty on N_{H} and an assumed uncertainty of ± 0.15 for E_{B-V} .

values: $\kappa_{\text{bol}} \gtrsim 300$ for the three weakly and undetected X-ray sources; and $\kappa_{\text{bol}} = 1350\text{--}2990$ for the strong detections J1216, J1234, and J1539. The κ_{bol} values for J1234 and J1539 are in agreement with previous estimates from Banerji et al. (2014) and Martocchia et al. (2017), respectively. Overall, the HRQs have higher bolometric corrections on average than expected from extrapolation of the $\kappa_{\text{bol}}\text{--}\lambda_{\text{Edd}}$ relation for lower luminosity AGNs.

3.4 λ_{Edd} versus N_{H} : radiation pressure feedback

Our sample of HRQs offers a unique opportunity to examine the picture of dusty radiative feedback. Firstly, the HRQs have the extreme luminosities (Section 3.3) and dust and gas columns in their circumnuclear environments (Section 3.2) that are expected for objects undergoing a blowout phase. Secondly, the absorption is significant but sufficiently low that the HRQs still have observable broad lines, which has allowed the measurement of black hole masses and Eddington ratios from the observed-frame near-IR spectra (Temple et al. 2019).

Powerful outflows are expected to be launched by black holes accreting at or above their Eddington luminosity, i.e. the threshold at which outward radiative forces match the inward gravitational pull. Dust enhances the effect of radiation pressure around AGNs, due to the effective absorption of UV light, and the coupling of dust and gas (e.g., Murray et al. 2005; Fabian et al. 2008; Thompson et al. 2015; Costa et al. 2018). This means that strong outflows are possible even at luminosities below the classic Eddington limit ($L_{\text{Edd}} = 1.3 \times 10^{38} M_{\text{BH}}/M_{\odot}$), which considers only a simple gas (e.g., Fabian et al. 2006, 2008; Roth et al. 2012). In

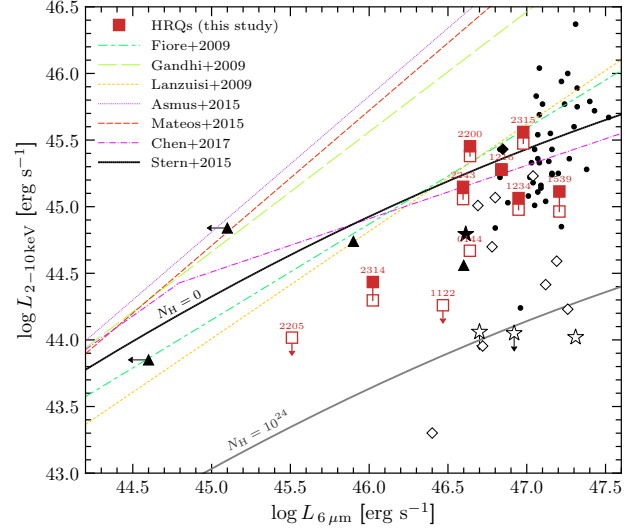


Figure 4. X-ray luminosity versus mid-infrared luminosity, for the HRQs (red squares) and other luminous quasar samples. Open shapes show absorbed X-ray luminosities and filled shapes show intrinsic (i.e., absorption-corrected) X-ray luminosities, obtained from X-ray spectral analyses. We compare with three other luminous reddened quasar samples: F2M red quasars (triangles; LaMassa et al. 2016b; Glikman et al. 2017); extremely red quasars (ERQs) from the SDSS (diamonds; Goulding et al. 2018); and WISE hot DOGs (stars; Stern et al. 2014; Vito et al. 2018a). For the latter two samples the intrinsic luminosities shown are averages from the analysis of stacked spectra. We also compare with a sample of the most luminous type 1 quasars known (small black circles; Martocchia et al. 2017), and intrinsic $L_{\text{X}}\text{--}L_{6\mu\text{m}}$ relations from a number of different AGN studies (as labelled). For the luminosity dependent relation of Stern (2015), we additionally show a modification of the relation (thick gray line) which shows the downscaling in X-ray luminosity expected for obscuration by Compton-thick gas ($N_{\text{H}} = 10^{24} \text{ cm}^{-2}$) along the line of sight.

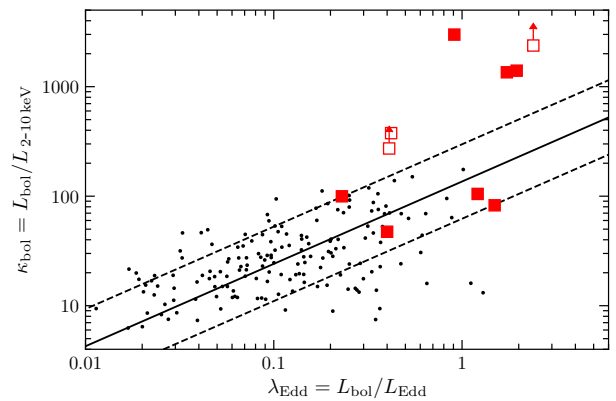


Figure 5. X-ray to bolometric correction (κ_{bol}) versus Eddington ratio (λ_{Edd}) for the HRQs (red squares). The black points, solid line, and dashed lines show Type 1 AGNs, their best fitting relation, and the 1σ dispersion, respectively, from Lusso et al. (2012).

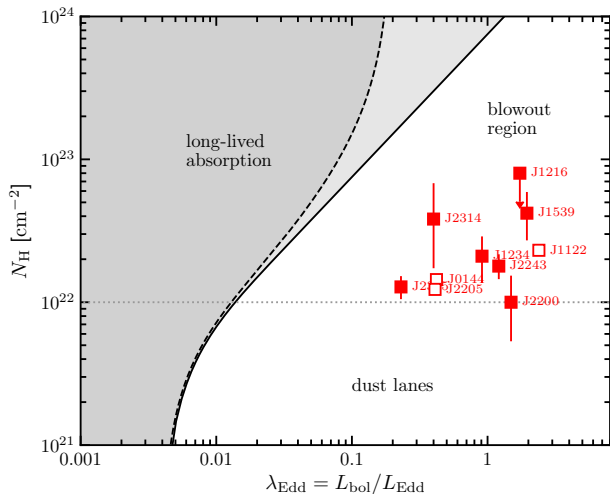


Figure 6. The $N_{\text{H}}-\lambda_{\text{Edd}}$ plane for HRQs, i.e., obscuring column density versus Eddington ratio ($\lambda_{\text{Edd}} = L_{\text{bol}}/L_{\text{Edd}}$). The tracks show the effective Eddington limit for dusty clouds in the cases of single scattering (solid line; e.g., Fabian et al. 2009) and radiation trapping (dashed line; Ishibashi et al. 2018), above which AGN are predicted to undergo a fast blowout phase. Below these limits, obscuring clouds may be long-lived. The horizontal dotted line marks $N_{\text{H}} = 10^{22} \text{ cm}^{-2}$, an approximate upper limit to the column density range expected for obscuration through host galaxy dust lanes.

other words, there is an effective Eddington limit for dusty gas, which is a function of the circumnuclear gas density (see the tracks in Figure 6).

In the low redshift Universe, there is evidence of this mechanism of radiation pressure feedback at work in AGNs. Hard X-ray selected AGN appear to preferentially avoid the “forbidden” (or “blowout”) region in the $N_{\text{H}}-\lambda_{\text{Edd}}$ plane, above the effective Eddington limit, where blowing out of the interstellar medium is expected (Fabian et al. 2009; Raimundo et al. 2010; Vasudevan et al. 2013; Ricci et al. 2017b; Bär et al. 2019; see also Ballo et al. 2014). Ricci et al. (2017b) demonstrated this for a large sample of 392 *Swift* BAT AGN ($\langle z \rangle = 0.037$), and showed that this physical connection between the obscuring environment of AGN and their accretion rates can help to explain observables such as the anticorrelation between obscured AGN fraction and luminosity (e.g., Burlon et al. 2011).

In Figure 6, we show the location of the X-ray observed HRQs on the $N_{\text{H}}-\lambda_{\text{Edd}}$ plane. We compare with tracks showing the effective Eddington limit for dusty gas, both in the single scattering limit (e.g., Fabian et al. 2009) and the radiation trapping limit (Ishibashi et al. 2018). Overall, the HRQ sample clearly lies above these limits, and thus in the blowout region. As usual for distant AGN, knowledge of the λ_{Edd} values is limited by the black hole mass measurements. For these sources the individual virial black hole masses have uncertainties of $\approx \pm 0.4$ dex (Temple et al. 2019). Some individual sources may therefore, in reality, lie closer to the effective Eddington limits. However, the large overall average offset observed of 1.5 dex from the solid line is difficult to explain by uncertainties alone. Alternatively, it is possible that systems appearing above the limit have obscuring ma-

terial at large distances, and are thus under the influence of a larger enclosed gravitational (stellar) mass, in which case the tracks in Figure 6 would move rightwards. The enclosed mass must be large ($\gtrsim 10M_{\text{BH}}$) for this to solely account for the HRQ data points.

3.4.1 Evidence for ongoing outflows

As shown above, the HRQs lie in the realm of $N_{\text{H}}-\lambda_{\text{Edd}}$ parameter space expected to be conducive to the driving of large-scale outflows via radiative pressure on dust. It is thus interesting to consider evidence for ongoing outflows. The X-ray spectra (Section 3.1) are not currently sufficient to place constraints on blueshifted emission around the Fe line complex. Future sensitive X-ray observations with high spectral resolution (e.g., with *Athena*) may be required to pick out such features. However, the observed-frame near-infrared spectra of the parent HRQ sample do show evidence for outflows. Specifically, broad components are identified in the emission line profiles of [O III] $\lambda 5007$.

Eight of the HRQs in this work have spectroscopic coverage of the [O III] and Balmer line complexes, which were modelled by Temple et al. (2019). In five cases [O III] is strongly detected, and in each case significant broadening of the [O III] line is measured. For four HRQs the 80% velocity width is large, with a range of $w_{80} = 1710\text{--}2572 \text{ km s}^{-1}$, and in two cases (J2200 and J2243) strong blueshifted wings are clearly observed in the [O III] line profiles. These are also the two cases with the highest signal-to-noise. For the remaining three sources (J0144, J1216, and J1234) [O III] is undetected, and appears to be intrinsically underluminous in the latter two sources. This is consistent with a picture where overionization or the expulsion of line-emitting gas results in weak emission from the narrow-line region (e.g., Temple et al. 2019; Netzer et al. 2004), and also with the finding that intrinsically weak [O III] emission is relatively common in high-luminosity high-redshift quasars compared to the lower redshift population (e.g., Coatman et al. 2019). There is further evidence for outflows in HRQs that currently lack X-ray coverage. For instance, assuming the average dust-to-gas ratios in Section 3.2, the two HRQs with the next highest N_{H} and λ_{Edd} values (J1117 and J1303) also exhibit very broad [O III] profiles ($w_{80} = 2277$ and 2898 km s^{-1} , respectively).

In summary, there is evidence for strong outflows of ionised gas around these HRQs, which may ultimately be connected to their location in the $N_{\text{H}}-\lambda_{\text{Edd}}$ diagram, thus linking the line kinematics to radiative feedback.

3.5 Comparison with other luminous quasar samples

Here we consider the results in the context of other relevant samples of highly luminous quasars which have been observed in the X-ray band. Figure 7 shows the $N_{\text{H}}-\lambda_{\text{Edd}}$ plane again, with the comparison samples plotted. We additionally compare with the lower luminosity, low-redshift AGN population selected by *Swift* BAT (Ricci et al. 2017b).

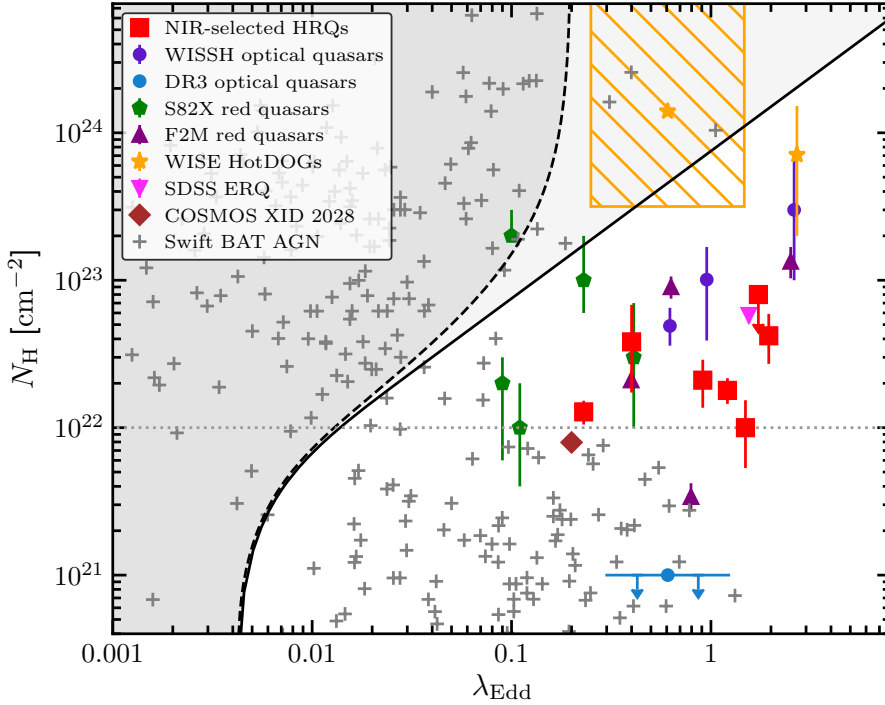


Figure 7. λ_{Edd} versus N_{H} , as in Figure 6. Here we compare with multiple different samples, and only show N_{H} constraints obtained from X-ray spectral modelling. In addition to our $z \approx 2.5$ HRQs, multiple other high luminosity reddened quasar samples are shown, including: *WISE* hot DOGs at $z \gtrsim 2$ (hatched orange region, based on Vito et al. 2018a and Wu et al. 2018); a $z = 1.0$ hot DOG (orange star; Ricci et al. 2017c); F2M red quasars at $z \approx 0.5$ (purple triangles; LaMassa et al. 2016b; Glikman et al. 2017); $z \approx 1$ red quasars in the Stripe 82 X-Ray Survey (green pentagons; LaMassa et al. 2017); an ERQ at $z = 2.3$ (magenta inverted triangle; Goulding et al. 2018; Perrotta et al. 2019); and the $z \approx 1.6$ dust-obscured quasar XID 2028 (brown diamond; Brusa et al. 2010; Kakkad et al. 2016). For hyperluminous optical quasars we show: the core ($\pm 1\sigma$) range of λ_{Edd} values for the most luminous quasars at $z \gtrsim 2$ in SDSS DR3 (blue line, plotted at $N_{\text{H}} = 10^{21} \text{ cm}^{-2}$); and the three $z \approx 2.5$ WISSH quasars mentioned in the text (purple circles; Martocchia et al. 2017). The “+” symbols show local ($z \approx 0.037$) *Swift* BAT AGN, which appear to avoid the blowout region (Ricci et al. 2017b; N_{H} uncertainties not plotted). The latter sample also contains many unobscured AGN at low N_{H} values, outside the range shown.

3.5.1 Reddened quasars

Comparable in luminosity ($L_{\text{bol}} \gtrsim 10^{46.6} \text{ erg s}^{-1}$) and redshift to our HRQs are the population of highly reddened hot dust-obscured galaxies (hot DOGs), selected from the mid-infrared *WISE* all-sky survey as “W1W2 dropouts”. Hot DOGs are so named due to hotter dust temperatures ($T \gg 60 \text{ K}$) with respect to ULIRGs, SMGs, and normal DOGs (Eisenhardt et al. 2012; Tsai et al. 2015; Assef et al. 2015). Similarly to HRQs, hot DOGs have comparable number densities to $z \gtrsim 2$ SDSS quasars at the highest luminosities ($L_{\text{bol}} \gtrsim 10^{47} \text{ erg s}^{-1}$; e.g., Assef et al. 2015). The most luminous hot DOGs lie at $z \approx 2-4$, are thought to be accreting close to the Eddington limit (e.g., Assef et al. 2015; Tsai et al. 2015, 2018; Wu et al. 2018), and are hidden by material which is either Compton-thick or highly obscured and Compton-thin (i.e., $N_{\text{H}} \gtrsim 10^{23.5} \text{ cm}^{-2}$; e.g., Stern et al. 2014; Piconcelli et al. 2015; Assef et al. 2016; Ricci et al. 2017c; Vito et al. 2018a; Zappacosta et al. 2018; Assef et al. 2019).

In Figure 7 we show a hatched region where the hot DOG population may lie, based on the column densities measured by Vito et al. (2018a) and assuming the Eddington ratio range measured by Wu et al. (2018; for a different subsample where broad lines are visible). We point out

that hot DOGs may reside in an interesting region of the $N_{\text{H}}-\lambda_{\text{Edd}}$ plane, below the Eddington limit for single scattering, but above the Eddington limit for radiation trapping. In other words, the high accretion rates of hot DOGs may lead to blowout due to radiative pressure feedback, but only if the infrared optical depth is sufficiently high (e.g., $\tau_{\text{IR}} \gg 1$; Ishibashi et al. 2018). The $z \approx 2$ hot DOGs studied by Wu et al. (2018) show some evidence for outflows in their optical emission lines. The most luminous hot DOG WISE J2246–0526 shows evidence for dramatic gas kinematics in the host galaxy, consistent with being due an emerging outflow driven by dusty radiation pressure feedback (e.g., Díaz-Santos et al. 2016).

Also comparable in luminosity and redshift are the extremely red quasars (ERQs; Ross et al. 2015; Hamann et al. 2017) which have been identified in the SDSS Baryon Oscillation Spectroscopic Survey (BOSS). This population at $z \approx 2-3$ is selected based on high infrared to optical flux ratios and high equivalent width C IV line emission. The sample is inconsistent with simple dust reddening, leading to a somewhat uncertain extinction ($E_{B-V} \gtrsim 0.3$; see discussion in Hamann et al. 2017). Goulding et al. (2018) presented the X-ray properties of ERQs, finding that they are mostly highly obscured or close to Compton-thick (e.g.,

$N_{\text{H}} \approx 8 \times 10^{23} \text{ cm}^{-2}$), and are likely obscured by their own equatorial outflows. Zakamska et al. (2016) and Perrotta et al. (2019) found dramatic fast [O III] outflows, reaching velocities up to $\approx 7000 \text{ km s}^{-1}$. We note that many ERQs are likely to lie in the blowout region, based on their expected N_{H} and λ_{Edd} values. In Figure 7 we plot one ERQ (SDSS J000610.67+121501.2) which has a constrained N_{H} (Goulding et al. 2018) and a λ_{Edd} measurement from Perrotta et al. (2019).

Glikman et al. (2012) presented a large sample of red quasars selected from FIRST and 2MASS with red optical to near-infrared colours. This population extends to the values of dust reddening, luminosity, and redshift found for our HRQs. Four of the lower redshift F2M quasars, with $z \approx 0.1\text{--}0.7$, $E_{B-V} = 0.6\text{--}1.5$, and $L_{6\mu\text{m}} = 10^{44.6\text{--}46.6} \text{ erg s}^{-1}$, have been studied with X-ray spectral modelling (LaMassa et al. 2016b; Glikman et al. 2017). The range of E_{B-V}/N_{H} values covered by the F2M quasars is similar to the HRQs. Glikman (2017) demonstrated that these lower redshift F2M quasars lie in the blowout region (as shown again here in Figure 7), and have merging host galaxies, thus reinforcing the picture that red quasars are a transitional radiatively driven blowout phase following a galaxy merger.

Red quasars have also been identified in X-ray surveys. As a notable example, the brightest obscured quasar in the COSMOS survey, XID 2028 ($z = 1.592$; $L_{\text{bol}} \approx 10^{46.3} \text{ erg s}^{-1}$; Brusa et al. 2010), also satisfies the red quasar criteria of Banerji et al. (2012). Followup of XID 2028 revealed outflows in multiple gas phases (e.g., Brusa et al. 2015a,b, 2016). Kakkad et al. (2016) showed that the quasar lies close to the blowout region, along with some other lower luminosity AGN exhibiting [O III] outflows, and we plot a data point for XID 2028 in Figure 7 for comparison.

In summary, HRQs and other luminous reddened quasar populations appear to occupy the forbidden blowout region, and simultaneously display other observational features (e.g., fast outflows) expected for a blowout phase. This potentially connects the kinematics in the quasar host galaxies to the underlying physical mechanism of AGN feedback during phases of extremely fast accretion onto supermassive black holes. Deeper, more detailed study of the populations in the blowout region will continue to help to establish the role of radiative pressure feedback in influencing galaxy properties, including the importance relative to other mechanisms of feedback from winds or jets (e.g., Veilleux et al. 2005; Wagner et al. 2016; Wylezalek & Morganti 2018; Jarvis et al. 2019).

3.5.2 Optical quasars

In addition to the reddened quasar samples discussed above, we consider the properties of comparably luminous unobscured (unreddened) quasars. The most luminous optical quasars in SDSS DR3 (with $M_i < -29.28$) were presented in Just et al. (2007) and Stern (2015), and include objects at $z \approx 2\text{--}3.5$, with $L_{6\mu\text{m}} \approx 10^{46.5\text{--}47.5} \text{ erg s}^{-1}$. A data point is shown in Figure 7 to highlight the core ($\pm 1\sigma$) range of Eddington ratios measured for these optical quasars. This is similar to the range of Eddington ratios found for the HRQs, but optical quasars typically have low intrinsic N_{H} values (as expected from their low dust reddening), meaning they generally lie well below red quasars in the $N_{\text{H}}\text{--}\lambda_{\text{Edd}}$ diagram.

Nevertheless, luminous optical quasars do show evidence of outflows. In fact, Temple et al. (2019) find no significant difference between the kinematic [O III] properties of HRQs and optical quasars when matching in luminosity and redshift. It may be that large-scale outflows, initially launched by radiation pressure during a reddened quasar phase, persist and remain observable at the time when the central engine is exposed as an optical quasar.

There are some cases, in exception to the above, of luminous optical quasars with relatively high N_{H} values, and which thus appear to lie in the blowout region. In Figure 7 we show, as an example, three such cases from the WISE/SDSS selected hyper-luminous (WISSH) quasar sample (Weedman et al. 2012; Bischetti et al. 2017; Martocchia et al. 2017). These three were identified by taking the X-ray studied WISSH sample of Martocchia et al. (2017; 41 sources overall), and taking the sources with: constrained N_{H} values; and λ_{Edd} estimates (from Shen et al. 2011) which place them in the blowout region. The remaining WISSH sources mostly have upper limits in column density (i.e., consistency with low N_{H}). The three sources shown, SDSS J132827.06+581836.8, J152156.48+520238.4, and J154938.71+124509.1, may be cases where the high N_{H} arises from dust-free gaseous absorption close to the nucleus. J1328 and J1549 both belong to the minority of (nine) WISSH sources studied by Martocchia et al. (2017) which are highlighted as being broad absorption line (BAL) quasars. In such systems, fast outflows occur along the line-of-sight, likely originating from winds around the inner accretion disk. The third source, J1521, is extremely luminous ($L_{\text{bol}} \approx 10^{48.2} \text{ erg s}^{-1}$) and belongs to the rare category of weak-line quasars (WLQs). In WLQs, a geometrically thick inner accretion disk is hypothesised to cause the gaseous X-ray obscuration (Wu et al. 2011; Luo et al. 2015). Considering the above, care should be taken when interpreting the location of a given source in the $N_{\text{H}}\text{--}\lambda_{\text{Edd}}$ plane, without consideration of the broader multiwavelength properties, such as dust to gas ratios.

3.5.3 Time evolution

Generally very few AGNs lie in the blowout region. This suggests that flickering to accretion rates above the effective Eddington limit is uncommon over short timescales, and that blowout (to lower N_{H} values) occurs relatively quickly. These HRQs may therefore represent a brief, but important, phase in an evolutionary sequence for massive galaxies (e.g., Hopkins et al. 2008; Somerville et al. 2008; Alexander & Hickox 2012; Bridge et al. 2013) driven by radiative pressure feedback (Ishibashi & Fabian 2016). In this picture, some quasars may graduate downwards in Figure 7: a deeply enshrouded Type 2 or hot DOG-like phase occurs, with accretion exceeding the effective Eddington limit due to a plentiful fuel supply (and hence high- N_{H}); the expulsion of material follows, resulting in a red quasar, and then finally an unobscured quasar phase. Wu et al. (2018) found this picture to be consistent with the black hole properties of these samples at $z \sim 2$. Some further support is added by observations of starbursts and merging host galaxies for the various populations (e.g., Urrutia et al. 2008; Glikman et al. 2015; Fan et al. 2016; Banerji et al. 2018; Diaz-Santos et al. 2018).

For a rough estimate of the timescale for blowout, given our measurements for HRQs, we consider the simplified case of an expanding shell of material. We assume that the matter is initially close to Compton-thick, with a column density of $N_{\text{H},0} = 10^{24} \text{ cm}^{-2}$, lies within an initial radius of $r_0 = 30 \text{ pc}$, and thus has a mass of $M \approx 4 \times 10^7 M_{\odot}$. Assuming that the column density evolves as $N_{\text{H}} \propto r^{-2}$ (e.g., Ishibashi & Fabian 2015),¹ the radius must increase by a factor of seven to reach the column densities observed for HRQs ($N_{\text{H}} \approx 2 \times 10^{22} \text{ cm}^{-2}$; Section 3.1). It follows that the timescale for this phase of the blowout is $t \approx 7 \times (3 \times 10^4 \text{ yr}) \times (\frac{r_0}{30 \text{ pc}})(\frac{v}{1000 \text{ km s}^{-1}})^{-1}$. In this simple picture, the obscuring material in HRQs should lie at radii of order $\sim 200 \text{ pc}$. This is in agreement with our results for the dust-to-gas ratios (Section 3.2), which suggest that the obscuration occurs on larger physical scales than in typical AGN. Future study should address how well this timescale for blowout agrees with the fraction of sources in the forbidden region, and the space densities of HRQs and other luminous quasars.

4 SUMMARY

We have reported on *XMM-Newton* observations of ten heavily dust-reddened quasars (HRQs), five of which are from recent new dedicated observations. This has allowed us to characterise the high-energy properties of HRQs at $\langle L_{\text{bol}} \rangle = 10^{47.5} \text{ erg s}^{-1}$ and $\langle z \rangle = 2.5$. These represent an important population of quasars, which are similar in number density to the most luminous unobscured (e.g., SDSS) quasars at these redshifts. Due to the high redshifts of the sources, we have been able to access energies of $E \approx 0.7\text{--}35 \text{ keV}$ in the source rest-frame, a range where the primary X-ray coronal emission is well sampled. Our main results are as follows:

- Of the five newly observed HRQs, three are well detected (J2200, J2243, and J2314) and two are undetected (J1122 and J2205) by *XMM-Newton* at 0.5–10 keV. Including the other $z > 2$ HRQs with X-ray coverage, this brings the total numbers of X-ray detected and undetected HRQs to eight and two, respectively; see Section 2.
- The measured gas column densities are in the range $N_{\text{H}} = (1\text{--}8) \times 10^{22} \text{ cm}^{-2}$, and the typical intrinsic (i.e., unabsorbed) photon index is found to be $\bar{\Gamma} \approx 1.9$. The intrinsic X-ray luminosities measured are $L_{2\text{--}10\text{keV}} = 10^{44.4\text{--}45.6} \text{ erg s}^{-1}$, with an average of $10^{45.1}$, confirming these as powerful AGNs in the X-ray band; see Section 3.1.
- We explore the dust to gas ratios in the extreme environments of the HRQs by determining E_{B-V}/N_{H} . The ratios measured (average of $E_{B-V}/N_{\text{H}} = 10^{-22.3}$) suggest a relatively high dust content for the obscurers, compared to other AGNs; see Section 3.2.
- The intrinsic X-ray luminosities ($L_{2\text{--}10\text{keV}}$) measured are weaker, relative to $L_{6\mu\text{m}}$ and L_{bol} , than is found for lower redshift, lower luminosity AGN. Broadly, this agrees with other hyperluminous quasar samples. However, the HRQs show tentative evidence for being even more (intrinsically) X-ray weak than other quasars of comparable luminosity.

¹ The evolution can be flatter, for instance, if this is the first outflowing shell and a significant amount of the ISM is swept up.

The X-ray to bolometric corrections reach up to extremely high values of $\kappa_{\text{bol}} > 1000$; see Section 3.3.

- We find that all of the HRQs are in agreement with moderate column densities and high Eddington ratios ($\lambda_{\text{Edd}} > 0.2$), placing them in a region of the $N_{\text{H}}\text{--}\lambda_{\text{Edd}}$ plane which is systematically avoided by X-ray survey samples (e.g., Ricci et al. 2017b). In this “forbidden” or “blowout” region, radiative pressure feedback acting on dusty gas is expected to drive strong outflows. In agreement with this picture, the narrow-line region ([O III]) properties of the HRQs studied here show evidence for ongoing outflows; see Section 3.4.

- Along with the HRQs, a number of other highly luminous quasar samples appear to lie in the blowout region for radiative pressure feedback. However, we note that the wider source properties (e.g., dust to gas ratios) must be considered when interpreting this. The locations of different samples in the $N_{\text{H}}\text{--}\lambda_{\text{Edd}}$ plane are broadly compatible with a picture where different populations are connected by an evolutionary sequence; see Section 3.5.

ACKNOWLEDGEMENTS

This work was supported by a Herchel Smith Research Fellowship of the University of Cambridge (G.B.L.); and ERC Advanced Grant 340442 (A.C.F.). We thank the anonymous referee for their review, which improved this work. Paul Hewett, Wako Ishibashi, Roberto Maiolino, and Richard McMahon are thanked for the useful discussions. This work is based on observations obtained with *XMM-Newton*, an ESA science mission with instruments and contributions directly funded by ESA Member States and NASA.

REFERENCES

- Aird J., Coil A. L., Georgakakis A., Nandra K., Barro G., Pérez-González P. G., 2015, *MNRAS*, **451**, 1892
- Alexander D. M., Hickox R. C., 2012, *New Astron. Rev.*, **56**, 93
- Alexander D. M., et al., 2013, *ApJ*, **773**, 125
- Arnaud K. A., 1996, in Jacoby G. H., Barnes J., eds, *Astronomical Society of the Pacific Conference Series Vol. 101, Astronomical Data Analysis Software and Systems V*. p. 17
- Asmus D., Gandhi P., Hönig S. F., Smette A., Duschl W. J., 2015, *MNRAS*, **454**, 766
- Assef R. J., et al., 2015, *ApJ*, **804**, 27
- Assef R. J., et al., 2016, *ApJ*, **819**, 111
- Assef R. J., et al., 2019, arXiv e-prints, p. arXiv:1905.04320
- Bañados E., et al., 2018, *ApJ*, **856**, L25
- Ballo L., Severgnini P., Della Ceca R., Caccianiga A., Vignali C., Carrera F. J., Corral A., Mateos S., 2014, *MNRAS*, **444**, 2580
- Baloković M., et al., 2018, *ApJ*, **854**, 42
- Banerji M., McMahon R. G., Hewett P. C., Alaghband-Zadeh S., Gonzalez-Solares E., Venemans B. P., Hawthorn M. J., 2012, *MNRAS*, **427**, 2275
- Banerji M., McMahon R. G., Hewett P. C., Gonzalez-Solares E., Kposov S. E., 2013, *MNRAS*, **429**, L55
- Banerji M., Fabian A. C., McMahon R. G., 2014, *MNRAS*, **439**, L51
- Banerji M., Alaghband-Zadeh S., Hewett P. C., McMahon R. G., 2015, *MNRAS*, **447**, 3368
- Banerji M., Jones G. C., Wagg J., Carilli C. L., Bisbas T. G., Hewett P. C., 2018, *MNRAS*, **479**, 1154
- Bär R. E., et al., 2019, *MNRAS*, **489**, 3073

- Bischetti M., et al., 2017, *A&A*, **598**, A122
- Bower R. G., Benson A. J., Malbon R., Helly J. C., Frenk C. S., Baugh C. M., Cole S., Lacey C. G., 2006, *MNRAS*, **370**, 645
- Bridge C. R., et al., 2013, *ApJ*, **769**, 91
- Brusa M., et al., 2010, *ApJ*, **716**, 348
- Brusa M., et al., 2015a, *MNRAS*, **446**, 2394
- Brusa M., et al., 2015b, *A&A*, **578**, A11
- Brusa M., et al., 2016, *A&A*, **588**, A58
- Burlon D., Ajello M., Greiner J., Comastri A., Merloni A., Gehrels N., 2011, *ApJ*, **728**, 58
- Burtscher L., et al., 2016, *A&A*, **586**, A28
- Carrera F. J., Fernández-Manteca P., Mateos S., 2017, in *Highlights on Spanish Astrophysics IX*. pp 120–124
- Chen C.-T. J., et al., 2017, *ApJ*, **837**, 145
- Coatman L., Hewett P. C., Banerji M., Richards G. T., Hennawi J. F., Prochaska J. X., 2019, *MNRAS*, **486**, 5335
- Costa T., Rosdahl J., Sijacki D., Haehnelt M. G., 2018, *MNRAS*, **479**, 2079
- Davies R. I., et al., 2015, *ApJ*, **806**, 127
- Debuhr J., Quataert E., Ma C.-P., 2011, *MNRAS*, **412**, 1341
- Díaz-Santos T., et al., 2016, *ApJ*, **816**, L6
- Díaz-Santos T., et al., 2018, *Science*, **362**, 1034
- Edge A., Sutherland W., Kuijken K., Driver S., McMahon R., Eales S., Emerson J. P., 2013, *The Messenger*, **154**, 32
- Eisenhardt P. R. M., et al., 2012, *ApJ*, **755**, 173
- Elvis M., et al., 1994, *ApJS*, **95**, 1
- Fabian A. C., 2012, *ARA&A*, **50**, 455
- Fabian A. C., Celotti A., Erlund M. C., 2006, *MNRAS*, **373**, L16
- Fabian A. C., Vasudevan R. V., Gandhi P., 2008, *MNRAS*, **385**, L43
- Fabian A. C., Vasudevan R. V., Mushotzky R. F., Winter L. M., Reynolds C. S., 2009, *MNRAS*, **394**, L89
- Fabian A. C., Lohfink A., Kara E., Parker M. L., Vasudevan R., Reynolds C. S., 2015, *MNRAS*, **451**, 4375
- Fan L., et al., 2016, *ApJ*, **822**, L32
- Ferrarese L., Merritt D., 2000, *ApJ*, **539**, L9
- Fiore F., et al., 2009, *ApJ*, **693**, 447
- Gandhi P., Horst H., Smette A., Hönig S., Comastri A., Gilli R., Vignali C., Duschl W., 2009, *A&A*, **502**, 457
- Gebhardt K., et al., 2000, *ApJ*, **539**, L13
- Glikman E., 2017, *Research Notes of the American Astronomical Society*, **1**, 48
- Glikman E., Helfand D. J., White R. L., Becker R. H., Gregg M. D., Lacy M., 2007, *ApJ*, **667**, 673
- Glikman E., et al., 2012, *ApJ*, **757**, 51
- Glikman E., Simmons B., Maily M., Schawinski K., Urry C. M., Lacy M., 2015, *ApJ*, **806**, 218
- Glikman E., LaMassa S., Piconcelli E., Urry M., Lacy M., 2017, *ApJ*, **847**, 116
- Goulding A. D., et al., 2018, *ApJ*, **856**, 4
- Güver T., Özel F., 2009, *MNRAS*, **400**, 2050
- Hainline K. N., Hickox R. C., Carroll C. M., Myers A. D., DiPompeo M. A., Trouille L., 2014, *ApJ*, **795**, 124
- Hamann F., et al., 2017, *MNRAS*, **464**, 3431
- Hickox R. C., Alexander D. M., 2018, *ARA&A*, **56**, 625
- Hönig S. F., 2019, *ApJ*, **884**, 171
- Hönig S. F., Kishimoto M., 2017, *ApJ*, **838**, L20
- Hopkins P. F., Hernquist L., Cox T. J., Kereš D., 2008, *ApJS*, **175**, 356
- Ichikawa K., Ueda Y., Terashima Y., Oyabu S., Gandhi P., Matsuta K., Nakagawa T., 2012, *ApJ*, **754**, 45
- Ishibashi W., Fabian A. C., 2015, *MNRAS*, **451**, 93
- Ishibashi W., Fabian A. C., 2016, *MNRAS*, **463**, 1291
- Ishibashi W., Fabian A. C., Ricci C., Celotti A., 2018, *MNRAS*, **479**, 3335
- Jarvis M. E., et al., 2019, *MNRAS*, **485**, 2710
- Just D. W., Brandt W. N., Shemmer O., Steffen A. T., Schneider D. P., Chartas G., Garmire G. P., 2007, *ApJ*, **665**, 1004
- Kakkad D., et al., 2016, *A&A*, **592**, A148
- Kalberla P. M. W., Burton W. B., Hartmann D., Arnal E. M., Bajaja E., Morras R., Pöppel W. G. L., 2005, *A&A*, **440**, 775
- Klindt L., Alexander D. M., Rosario D. J., Lusso E., Fotopoulou S., 2019, *MNRAS*, **488**, 3109
- Kraft R. P., Burrows D. N., Nousek J. A., 1991, *ApJ*, **374**, 344
- LaMassa S. M., et al., 2016a, *ApJ*, **817**, 172
- LaMassa S. M., et al., 2016b, *ApJ*, **820**, 70
- LaMassa S. M., et al., 2017, *ApJ*, **847**, 100
- Lansbury G. B., et al., 2014, *ApJ*, **785**, 17
- Lanzuisi G., Piconcelli E., Fiore F., Feruglio C., Vignali C., Salvato M., Gruppioni C., 2009, *A&A*, **498**, 67
- Lawrence A., et al., 2007, *MNRAS*, **379**, 1599
- Levenson N. A., Radomski J. T., Packham C., Mason R. E., Schaefer J. J., Telesco C. M., 2009, *ApJ*, **703**, 390
- Liu T., et al., 2018, *MNRAS*, **479**, 5022
- Luo B., et al., 2014, *ApJ*, **794**, 70
- Luo B., et al., 2015, *ApJ*, **805**, 122
- Lusso E., et al., 2012, *MNRAS*, **425**, 623
- Lutz D., Maiolino R., Spoon H. W. W., Moorwood A. F. M., 2004, *A&A*, **418**, 465
- Magorrian J., et al., 1998, *AJ*, **115**, 2285
- Maiolino R., Marconi A., Salvati M., Risaliti G., Severgnini P., Oliva E., La Franca F., Vanzì L., 2001, *A&A*, **365**, 28
- Martocchia S., et al., 2017, *A&A*, **608**, A51
- Mateos S., et al., 2015, *MNRAS*, **449**, 1422
- McMahon R. G., Banerji M., Gonzalez E., Kuposov S. E., Bejar V. J., Lodieu N., Rebolo R., VHS Collaboration 2013, *The Messenger*, **154**, 35
- Merloni A., et al., 2014, *MNRAS*, **437**, 3550
- Murray N., Quataert E., Thompson T. A., 2005, *ApJ*, **618**, 569
- Narayanan D., et al., 2010, *MNRAS*, **407**, 1701
- Netzer H., Shemmer O., Maiolino R., Oliva E., Croom S., Corbett E., di Fabrizio L., 2004, *ApJ*, **614**, 558
- Perrotta S., Hamann F., Zakamska N. L., Alexand roff R. M., Rupke D., Wylezalek D., 2019, *MNRAS*, **488**, 4126
- Piconcelli E., et al., 2015, *A&A*, **574**, L9
- Raimundo S. I., Fabian A. C., Bauer F. E., Alexander D. M., Brandt W. N., Luo B., Vasudevan R. V., Xue Y. Q., 2010, *MNRAS*, **408**, 1714
- Ricci C., et al., 2017a, *ApJS*, **233**, 17
- Ricci C., et al., 2017b, *Nature*, **549**, 488
- Ricci C., et al., 2017c, *ApJ*, **835**, 105
- Richards G. T., et al., 2003, *AJ*, **126**, 1131
- Richards G. T., et al., 2006, *AJ*, **131**, 2766
- Rivers E., Markowitz A., Rothschild R., 2013, *ApJ*, **772**, 114
- Ross N. P., et al., 2015, *MNRAS*, **453**, 3932
- Roth N., Kasen D., Hopkins P. F., Quataert E., 2012, *ApJ*, **759**, 36
- Sanders D. B., Mirabel I. F., 1996, *ARA&A*, **34**, 749
- Savage B. D., Mathis J. S., 1979, *ARA&A*, **17**, 73
- Shen Y., et al., 2011, *ApJS*, **194**, 45
- Shimizu T. T., et al., 2018, *ApJ*, **856**, 154
- Somerville R. S., Hopkins P. F., Cox T. J., Robertson B. E., Hernquist L., 2008, *MNRAS*, **391**, 481
- Springel V., Di Matteo T., Hernquist L., 2005, *ApJ*, **620**, L79
- Stern D., 2015, *ApJ*, **807**, 129
- Stern D., et al., 2014, *ApJ*, **794**, 102
- Temple M. J., Banerji M., Hewett P. C., Coatman L., Maddox N., Peroux C., 2019, *MNRAS*, **487**, 2594
- Teng S. H., et al., 2014, *ApJ*, **785**, 19
- Thompson T. A., Fabian A. C., Quataert E., Murray N., 2015, *MNRAS*, **449**, 147
- Toba Y., Ueda Y., Matsuoka K., Shidatsu M., Nagao T., Terashima Y., Wang W.-H., Chang Y.-Y., 2019, *MNRAS*, **484**, 196
- Tsai C.-W., et al., 2015, *ApJ*, **805**, 90
- Tsai C.-W., et al., 2018, *ApJ*, **868**, 15

- Urrutia T., Lacy M., Becker R. H., 2008, *ApJ*, **674**, 80
- Vasudevan R. V., Fabian A. C., 2007, *MNRAS*, **381**, 1235
- Vasudevan R. V., Mushotzky R. F., Winter L. M., Fabian A. C., 2009, *MNRAS*, **399**, 1553
- Vasudevan R. V., Brandt W. N., Mushotzky R. F., Winter L. M., Baumgartner W. H., Shimizu T. T., Schneider D. P., Nousek J., 2013, *ApJ*, **763**, 111
- Veilleux S., Cecil G., Bland-Hawthorn J., 2005, *ARA&A*, **43**, 769
- Vito F., et al., 2018a, *MNRAS*, **474**, 4528
- Vito F., Brandt W. N., Luo B., Shemmer O., Vignali C., Gilli R., 2018b, *MNRAS*, **479**, 5335
- Wagner A. Y., Bicknell G. V., Umemura M., Sutherland R. S., Silk J., 2016, *Astronomische Nachrichten*, **337**, 167
- Weedman D., Sargsyan L., Leboutteiller V., Houck J., Barry D., 2012, *ApJ*, **761**, 184
- Wethers C. F., et al., 2018, *MNRAS*, **475**, 3682
- Wu J., et al., 2011, *ApJ*, **736**, 28
- Wu J., et al., 2018, *ApJ*, **852**, 96
- Wylezalek D., Morganti R., 2018, *Nature Astronomy*, **2**, 181
- Zakamska N. L., et al., 2016, *MNRAS*, **459**, 3144
- Zappacosta L., et al., 2018, *A&A*, **618**, A28

This paper has been typeset from a $\text{\TeX}/\text{\LaTeX}$ file prepared by the author.